Opto-Electronic Science

ISSN 2097-0382 CN 51-1800/O4

Photonics-assisted THz wireless communication enabled by wide-bandwidth packaged back-illuminated modified uni-traveling-carrier photodiode

Yuxin Tian, Boyu Dong, Yaxuan Li, Bing Xiong, Junwen Zhang, Changzheng Sun, Zhibiao Hao, Jian Wang, Lai Wang, Yanjun Han, Hongtao Li, Lin Gan, Nan Chi and Yi Luo

Citation: Tian YX, Dong BY, Li YX, et al. Photonics-assisted THz wireless communication enabled by wide-bandwidth packaged back-illuminated modified uni-traveling-carrier photodiode. *Opto-Electron Sci* **3**, 230051 (2024).

https://doi.org/10.29026/oes.2024.230051

Received: 26 December 2023; Accepted: 9 April 2024; Published online: 1 July 2024

Related articles

Highly efficient vectorial field manipulation using a transmitted tri-layer metasurface in the terahertz band

Huan Zhao, Xinke Wang, Shutian Liu, Yan Zhang

Opto-Electronic Advances 2023 **6**, 220012 doi: 10.29026/oea.2023.220012

Unraveling the efficiency losses and improving methods in quantum dot-based infrared up-conversion photodetectors

Jiao Jiao Liu, Xinxin Yang, Qiulei Xu, Ruiguang Chang, Zhenghui Wu, Huaibin Shen

Opto-Electronic Science 2024 **3**, 230029 doi: 10.29026/oes.2024.230029

High-speed multiwavelength InGaAs/InP quantum well nanowire array micro-LEDs for next generation optical communications

Fanlu Zhang, Zhicheng Su, Zhe Li, Yi Zhu, Nikita Gagrani, Ziyuan Li, Mark Lockrey, Li Li, Igor Aharonovich, Yuerui Lu, Hark Hoe Tan, Chennupati Jagadish, Lan Fu

Opto-Electronic Science 2023 **2**, 230003 doi: 10.29026/oes.2023.230003

Efficient stochastic parallel gradient descent training for on-chip optical processor

Yuanjian Wan, Xudong Liu, Guangze Wu, Min Yang, Guofeng Yan, Yu Zhang, Jian Wang

Opto-Electronic Advances 2024 **7**, 230182 doi: 10.29026/oea.2024.230182

More related article in Opto-Electronic Journals Group website

Opto-Electronic Science

http://www.oejournal.org/oes

OE_Journal

Website

Opto-Electronic Science

Article

July 2024, Vol. 3, No. 7

DOI: 10.29026/oes.2024.230051

Photonics-assisted THz wireless communication enabled by wide-bandwidth packaged back-illuminated modified uni-traveling-carrier photodiode

Yuxin Tian[1†], Boyu Dong[2†], Yaxuan Li[2], Bing Xiong[1*], Junwen Zhang[2*], Changzheng Sun[1], Zhibiao Hao[1], Jian Wang[1], Lai Wang[1], Yanjun Han[1,3], Hongtao Li[1], Lin Gan[1], Nan Chi[2] and Yi Luo[1,3]

This paper presents a wide-bandwidth back-illuminated modified uni-traveling-carrier photodiode (MUTC-PD) packaged with standard WR-5 rectangular waveguide for high-speed wireless communications. With optimized epitaxy structure and coplanar waveguide electrodes, the fabricated 4-μm-diameter PD exhibits ultra-flat frequency response and high saturation power. Integrated passive circuits including low-loss bias-tee and E-plane probe are designed to package the PD into a compact module with waveguide output. The packaged PD module has demonstrated a flat frequency response with fluctuations within ±2.75 dB over a broadband of 140–220 GHz and a high saturated output power of −7.8 dBm (166 μW) at 140 GHz. For wireless communication applications, the packaged PD is used to implement 1-m free space transmission at carrier frequencies of 150.5 and 210.5 GHz, with transmission rates of 75 and 90 Gbps, respectively.

Keywords: modified uni-traveling-carrier photodiode; integrated bias-tee; E-plane probe; flat frequency response; high saturation power; WR-5 output; THz wireless communications

Tian YX, Dong BY, Li YX et al. Photonics-assisted THz wireless communication enabled by wide-bandwidth packaged back-illuminated modified uni-traveling-carrier photodiode. *Opto-Electron Sci* **3**, 230051 (2024).

Introduction

With the rapid development of high bit-rate wireless services driven by mobile internet, AI computing, high-definition videos, virtual reality/augmented reality (VAR) applications, and so on, the demand for wireless data rates has grown explosively in the past decades[1,2]. Supporting such fast data rate at tens of Gbit/s pushes the carrier frequency to the THz (0.1–10 THz) domain in 6G to accommodate the bandwidth-hungry wireless services[3–14]. Recently, considerable efforts have been invested in developing photonic techniques targeting ultrafast data rate wireless communication at THz

[1]Beijing National Research Center for Information Science and Technology (BNRist), Department of Electronic Engineering, Tsinghua University, Beijing 100084, China; [2]Key Laboratory of Information Science of Electromagnetic Waves (MoE), Department of Communication Science and Engineering, Fudan University, Shanghai 200433, China; [3]Flexible Intelligent Optoelectronic Device and Technology Center, Institute of Flexible Electronics Technology of THU, Jiaxing 314000, China.

†These authors contributed equally to this work.

*Correspondence: B Xiong, E-mail: bxiong@tsinghua.edu.cn; JW Zhang, E-mail: junwenzhang@fudan.edu.cn

Received: 26 December 2023; Accepted: 9 April 2024; Published online: 1 July 2024

frequencies[15–18].

Photodiodes (PDs) serve as a key component of photonic transmitter to realize optical-to-electrical conversion. In particular, uni-traveling-carrier photodiodes (UTC-PDs) have been developed to simultaneously achieve both ultrawide bandwidth and high output power[19]. For instance, flip-chip-bonded 6-μm-diameter UTC-PD has demonstrated bandwidth exceeding 110 GHz as well as radio frequency (RF) power of 7.8 dBm at 110 GHz[20]. Flip-chip bonded modified UTC-PDs (MUTC-PDs) exhibiting a 3-dB bandwidth up to 120 GHz or a saturated RF output power of −2.6 dBm at 160 GHz have also been reported[21].

Module packaging of high-speed PDs is important for their applications in millimeter wave or THz wireless communications. Packaging of GHz-bandwidth PDs is relatively mature. For example, fully packaged PD modules with coaxial connectors for below 30 GHz applications have been reported[22,23]. However, at frequencies over 100 GHz, high transmission losses as well as parasitic modes and resonances due to the packaging structure will seriously degrade the performance of PD modules. By adopting a conductor-backed coplanar waveguide (CBCPW) to suppress mode-mismatch between the PD and the RF connector, a packaged PD with 1-mm coaxial connector was reported to exhibit a bandwidth over 90 GHz[24]. A bandwidth of 145 GHz was estimated for a packaged PD equipped with 0.8-mm coaxial connector, but the frequency response exhibited a significant roll-off above 130 GHz[25].

For PD modules operating at higher frequencies, waveguide-integrated PD modules offer a promising solution for high-power THz output due to the low-loss nature of rectangular waveguides and the availability of a wide range of standard components. For instance, a WR-6 waveguide packaged UTC-PD module for D-band (110–170 GHz) operation was developed, with an output power around −5 dBm[26]. A WR3-band (220–320 GHz) PD module containing an MUTC-PD with short-stub resonant matching circuit was reported to achieve a maximum output power of 134 μW at 264 GHz[27].

Currently, many researchers have employed commercial UTC-PDs to construct photonic-assisted THz wireless communication systems, in which THz signals can be generated by beating two lasers with different wavelengths at the transmitting end. A demonstration showcased a multichannel THz wireless transmission utilizing the quadrature phase shift keying (QPSK) modulation format at a carrier frequency of 200 GHz, achieving a data rate of up to 75 Gbps[28]. In another experiment[29], a single-input single-output (SISO) wireless link was established at 237.5 GHz by utilizing a remote UTC-PD. Through the combination of modulation formats, such as QPSK and quadrature amplitude modulation (QAM), a maximum data rate of 100 Gbps was attained. Simultaneous photonic-assisted THz communication in three bands (150, 250, and 325 GHz) has also been demonstrated[30]. The net data rates reached 59.813, 74.766, and 93.333 Gbps, respectively.

In this work, we report a WR-5 waveguide packaged PD module for THz communications. The module contains a 4-μm-diameter back-illuminated MUTC-PD with optimized epitaxy structure and coplaner waveguide (CPW) electrodes to ensure wide bandwidth and high saturation power. Passive circuits including bias-tee and E-plane probe are incorporated into the module. The packaged PD module has demonstrated a flat frequency response with fluctuations within ±2.75 dB in the entire G-band, and the saturated output power reaches −7.8 dBm at 140 GHz.

Photonics-assisted THz wireless communication experiment have been caried out. Thanks to the high saturation power and high conversion efficiency of the PD module, meter level short distance wireless data transmission has been demonstrated without additional power amplifiers after the optical-to-electrical conversion. To ensure high-performance signal transmission and avoid nonlinear effects caused by the MUTC-PD under high optical power, the 8- amplitude phase shift keying (APSK) modulation format is employed, and transmission rates of 75 and 90 Gbps over 1-m free space at 150.5 and 210.5 GHz carrier frequencies, respectively, are demonstrated.

PD chip design and fabrication

The epitaxial structure of our MUTC-PD is shown in Fig. 1(a), similar to the one reported in our previous work[31]. A gradient-doped absorption layer is employed to alleviate the space charge effect for improved saturation performance, while a cliff layer with optimized doping is adopted to sustain electron velocity overshoot for enhanced bandwidth. Inductive peaking can be implemented with high-impedance CPW to manipulate the frequency response, enabling a reduced power roll-off at the high frequencies of interest. As shown in Fig. 1(b), a flat output power over 140–220 GHz can be maintained

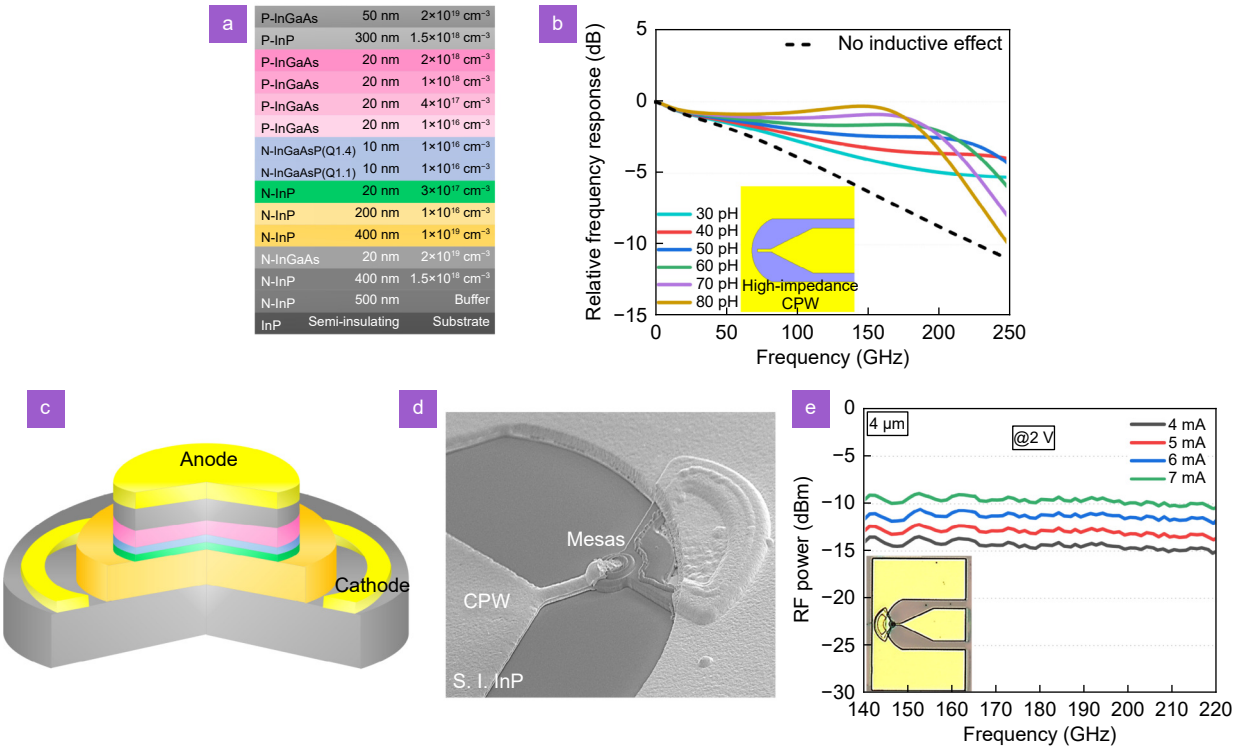

Fig. 1 | (**a**) Epitaxy structure of the proposed MUTC-PD. (**b**) Influence of high-impedance CPW inductance on frequency response of the 4-μm-diameter PD. (**c**) 3D schematic view of the PD. (**d**) SEM image of the fabricated device. (**e**) Frequency responses under various photocurrents of the 4-μm-diameter PD under 2 V bias voltage.

when the inductance is designed to 50 pH (5E-11H).

The 3D schematic of the 4-μm-diameter PD is illustrated in Fig. 1(c), which adopts a triple-mesa structure for improved fabrication yield and consistency. The first mesa is etched by inductive coupled plasma (ICP) and stopped slightly below the p-n junction to load most of the electric field. The second mesa is defined by a combination of dry-etching and wet-etching process[31]. Diluted HCl is used to stop precisely at the InGaAs layer for ohmic contact formation. The bottom mesa is etched down to the semi-insulating InP substrate to provide insulation. Ti/Pt/Au and Ni/Au electrodes are formed on the p- and n-contact layers by magnetron sputtering. Scanning electron microscope (SEM) image of the fabricated device is shown in Fig. 1(d). Due to the relatively complex fabrication process, the performance of PDs on the same wafer may vary somewhat.

The frequency response of the fabricated 4-μm-diameter MUTC-PD at G-band are measured with a two-laser heterodyne system. The frequency responses under different photocurrents with a fixed reverse bias of 2 V are plotted in Fig. 1(e). The PD exhibits ultra-flat frequency responses over the entire G-band under various photocurrents, together with a responsivity of 0.07 A/W. The saturation characteristics of the PD is not measured, as the PD performance might deteriorate after the high-photocurrent saturation measurement, which will affect the evaluation of the frequency responses of the PD after packaging.

Design of passive circuits

To package the high-speed PD chip into a compact module with waveguide output, it is essential to realize smooth transition from the CPW electrodes on the PD to the waveguide port. In addition, a bias-tee is also required to provide dc bias to the module. These are implemented by passive circuits formed on 127-μm-thick quartz substrate, which is adopted for reduced dielectric loss at high frequencies. The configuration of the passive circuits is illustrated in Fig. 2(a).

A novel bias-tee is proposed and fabricated based on interdigital structure coplanar waveguide, securing broadband and low loss transmission at G-band compared with the commonly reported bias-tee structures[32–34]. The bias-tee consists of an RF-choke and a DC-block. The RF-choke is formed by an interdigital inductor[35], which serves as a quarter wavelength transformer, resulting in a virtual RF open circuit. Two open

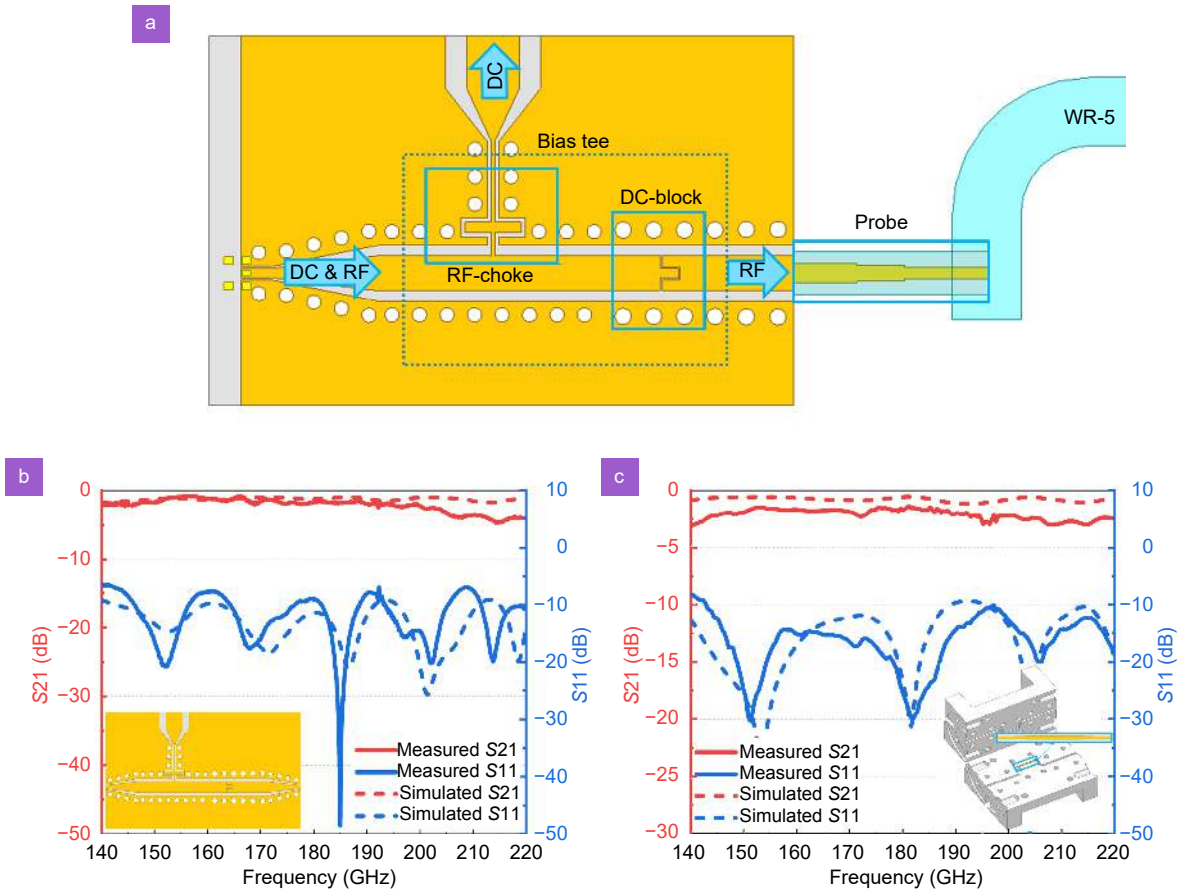

Fig. 2 | (**a**) Top view of passive circuits consist of interdigital inductor-based RF-choke, interdigital capacitor-based DC-block and E-plane probe. Measurement and simulation results of the back-to-back (**b**) bias-tee and (**c**) probe package.

circuit stubs in parallel are employed to improve the RF signal isolation[36]. The DC-block is formed by an interdigital capacitor[35] to ensure low loss and smooth transition over wideband, whereas traditional coupled-line based DC-block exhibits bandpass performance[34]. The bias-tee performance is test by microwave probes via a back-to-back configuration, as shown in Fig. 2(b). The measured insertion loss (IL) is less than 4 dB, while the return loss (RL) is about 10 dB. The measurements are in reasonable agreement with the simulation results.

In previous studies, the planar transmission line to rectangular waveguide transition at D-band employing wire bonding probe[37] or metal ridge[38] suffers from poor repeatability and large loss. The transition implemented by a stepped-impedance E-plane probe converts the quasi-TEM mode of the microstrip to the dominant TE_{10} mode in the waveguide with low loss. Smooth transition over the G-band is realized through impedance matching by varying the width of microstrip in three steps. A back-to-back package is fabricated to verify the performance of the E-plane probe. As plotted in Fig. 2(c), an RL over 10 dB is recorded over the G band, while the measured IL is around 2.25 dB, corresponding to an IL of 1.125 dB for a single microstrip-to-waveguide transition. Again, the measurement results are in fair agreement with the simulations.

WR-5 module packaging and characterization

The schematic of the PD module with WR-5 waveguide output is shown in Fig. 3(a). The PD chip is flip-chip bonded to the passive circuits including bias-tee, E-plane probe and DC components. An electrostatic discharge (ESD) chip is included in the DC path, so as to protect the chip against static electric damage. A lensed fiber is used to couple light into the PD, and the converted THz signal is extracted through a WR-5 waveguide.

During the package, planar passive circuits, including the bias-tee and the E-plane probe, are first fixed onto the bottom block of the module by silver-filled epoxy. Gold-wire bonding is employed for chip-level interconnections, as shown in Fig. 3(b). The length and height of

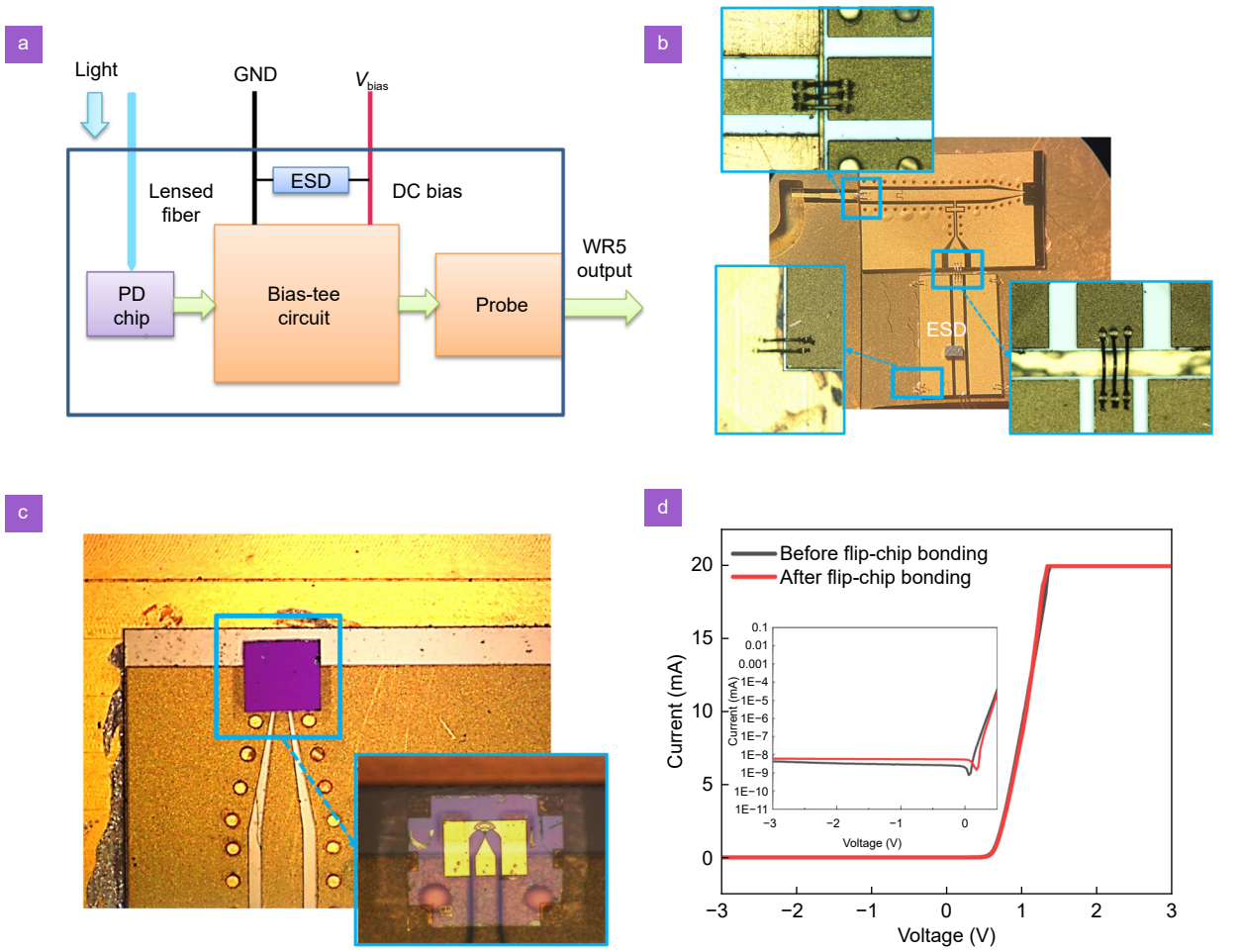

Fig. 3 | (**a**) Schematic of the WR-5 packaged PD module. ESD: electro static discharge. (**b**) Wire-bonding interconnection of the passive circuits. (**c**) Microscope photo of the flip-chip bonded PD chip. (**d**) I-V characteristics before and after flip-chip bonding.

the bonding wires are kept at a minimum so as to suppress parasitic inductance.

Next, the PD chip is flip-chip bonded to the passive circuits via gold bumps formed at the end of the bias-tee, as shown in Fig. 3(c). The flip-chip bonding conditions is optimized to ensure that no degradation in PD performances occur during bonding. As plotted in Fig. 3(d), the I-V characteristics, including dark current and contact resistance remain almost unvaried after the flip-chip bonding. As the final step, a lensed fiber is attached to the PD module to ensure best responsivity.

The fully packaged MUTC-PD with standard WR-5 output is shown in Fig. 4(a). The frequency responses tested under a reverse bias of 2 V are plotted in Fig. 4(b). The PD module exhibits a flat frequency response with a fluctuation within ±2.75 dB over 140–220 GHz under various photocurrents. Compared with Fig. 1(e), the packaged PD shows a power drop by about 1.09 dB, which is consistent with the insertion losses of the bias-tee and the probe, indicating that no additional losses are introduced during the packaging process. The frequency-dependent saturation characteristics of the packaged PD is shown in Fig. 4(c). The saturation photocurrent under 140, 150, and 160 GHz is 8.6, 8.3, 7.7 mA, corresponding to a saturation power of −7.8, −8.3, and −8.9 dBm, respectively. Figure 5 summarizes the saturation output power versus the operation frequency of UTC-PD modules reported in the literature. The proposed MUTC-PD module with rectangular waveguide output shows high saturation power at high frequencies without employing resonant matching circuits.

Application to wireless communications

Experimental setup

The MUTC-PD has great potential for applications in photonic-assisted THz wireless communications. The flat response over the G-band enables easy frequency agility at the transmitting end, making it suitable for diverse application scenarios. Experiments are carried out

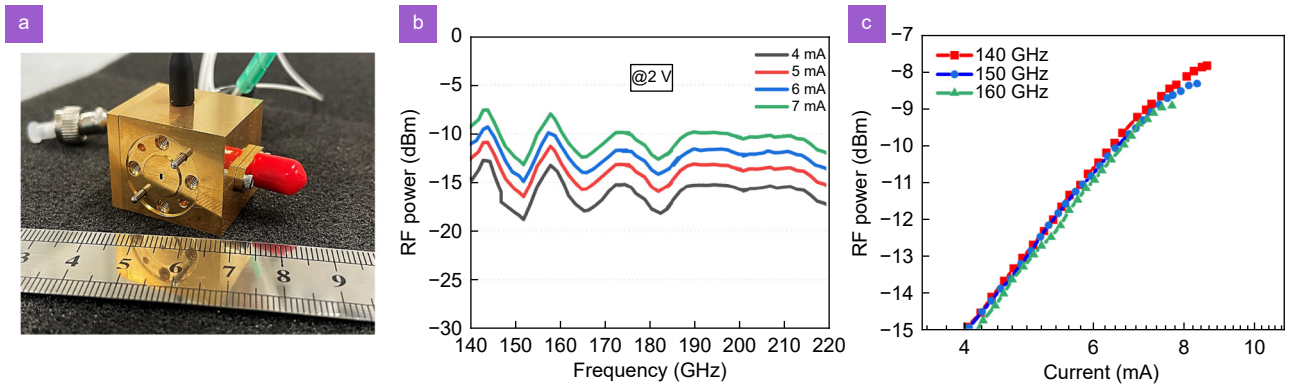

Fig. 4 | (**a**) The packaged WR-5 MUTC-PD module. (**b**) Frequency response under various photocurrents and (**c**) frequency-dependent saturation characteristics at 2 V bias voltage of WR-5 PD module.

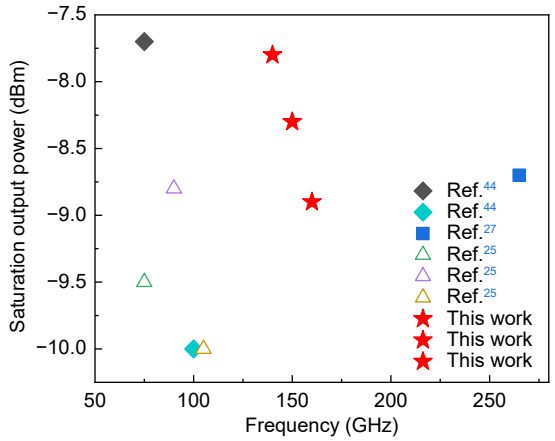

Fig. 5 | Comparison of saturation output power against operation frequency for packaged UTC-PD modules. Open marks are for coaxial output modules, and closed ones for waveguide output modules. The rectangular mark indicates module with resonant matching circuit.

to showcase the ultra-broad bandwidth MUTC-PD module in a photonic-assisted THz high-speed wireless communication system.

Figure 6 provides an overview of the photonic-assisted THz high-speed wireless communication system and the offline digital signal processing (DSP). The first step in the transmission process involves generating and mapping the data sequence according to regular 8-APSK. The baseband signal then undergoes up-sampling and pulse-shaping using a root-raised cosine filter with a roll-off factor of 0.1. The resulting baseband signal, depicted in Fig. 6(a), is then sent to an arbitrary waveform generator (AWG) with a sampling rate of 64 GSa/s. Subsequently, the signal is modulated onto the light emitted by an external cavity laser (ECL) using an IQ modulator. ECL-1, operating at 193.3985 THz with a linewidth of 100 kHz, serves as the light source for this system. Finally, the signal light is amplified by an erbium-doped fiber amplifier (EDFA) and aligned with the polarization state of the local oscillator (LO) light emitted by ECL-2 through a polarization controller.

In the experiment, the frequencies of the light emitted by ECL-2 are set to 193.549 and 193.609 THz, respectively, to verify the ultra-broadband response of the MUTC-PD module and its application in frequency agile THz communication systems. The optical spectra recorded after the optical coupler (OC) are shown in Fig. 6(b) and 6(c), revealing a frequency difference of 150.5 and 210.5 GHz between the two lasers, respectively. Subsequently, the light coming out of the OC is amplified by another EDFA and fed into the MUTC-PD module. The generated THz signal is then launched by the horn antenna (HA). The high saturation power and high conversion efficiency of the PD module enables meter-level short distance THz communication transmission without the need for additional power amplifiers. For effective transmission of THz signals at different frequencies, HAs with different center frequencies are employed at the transmitting end.

At the receiving end, receivers at different frequency bands are adopted to receive THz signals at 150 and 210 GHz, respectively. After 1-m wireless link transmission, the transmitted THz signal is captured by the HA, amplified by a low noise amplifier (LNA), and then mixed with the LO signal generated by frequency multiplier. The signal is down-converted to the intermediate frequency (IF) after passing through the mixer. The IF signal is then amplified by an electrical amplifier (EA) and captured by an oscilloscope (OSC) at a sampling rate of 80 GSa/s. Subsequently, the captured signal is processed using an offline DSP to recover the original data. The offline DSP mainly includes down-conversion, matched filtering, down-sampling, and some traditional coherent

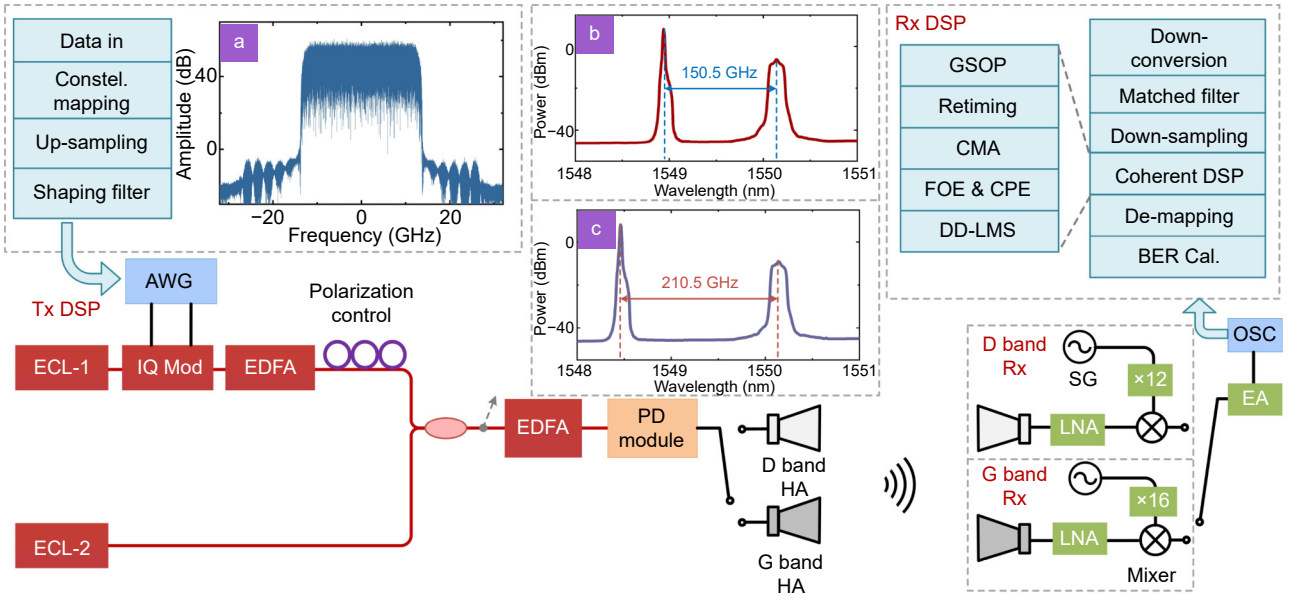

Fig. 6 | Experimental setup of THz wireless communication with the proposed MUTC-PD. AWG: arbitrary waveform generator, ECL: external cavity laser, IQ Mod: IQ modulator, OC: optical coupler, SG: signal generator, LNA: low noise amplifier, EA: electrical amplifier, OSC: oscilloscope, SG: signal generator. (**a**) Spectrum of the transmitting signal with 25 G Baud. (**b**) Optical spectrum of the OC at a frequency difference of 150.5 GHz between two lasers. (**c**) Optical spectrum of the OC at a frequency difference of 210.5 GHz between two lasers.

communication DSP, as shown in Fig. 6. As the first step, the Gram-Schmidt orthogonal projection (GSOP) is adopted to correct the I/Q imbalance, followed by clock recovery based on the fast square-timing-recovery algorithm. The signal is recovered by blind equalization based on the constant modulus algorithm (CMA). Following the frequency offset and carrier phase estimation (FOE & CPE), a decision-directed least mean square (DD-LMS) algorithm is employed to further enhance the system performance. Finally, the signal undergoes APSK demodulation, and the error vector magnitude (EVM) is calculated.

Results and discussion

The modulation format adopted in the experiment is 8-APSK, which offers improved frequency spectral efficiency and achieves a higher data rate compared with common low-order modulation formats, such as OOK or QPSK. Furthermore, the 8-APSK modulation scheme demonstrates superior resistance to nonlinear distortion compared to the standard 8-QAM modulation scheme. Figure 7 shows the EVM performance of the 8-APSK signals transmitted over a 1-m wireless distance at different baud rates at the center carrier frequencies of 150.5 GHz and 210.5 GHz, respectively. In our experiment, bit-error-free transmission of 5-GHz baud rate 8-APSK signals are verified at both 150.5 GHz and 210.5 GHz. At 150.5 GHz carrier frequency, the system can support transmission at 25-GHz baud rate below the forward-error-correction (FEC) threshold of 1E-2, corresponding to a transmission rate of 75 Gb/s. The bit-error-rate (BER) value is 9.66E-3 and the EVM value is 26.92%. Similarly, over 30-GHz baud rate transmission can be achieved at 210.5 GHz, with the EVM value of 26.71% and BER value of 9.06E-3. In the experiment, we also endeavored to attain higher data rates by employing a high-order QAM scheme. Specifically, we conducted the THz wireless communication experiment utilizing a 20-GHz baud rate standard 16-QAM signal at a carrier frequency of 150.5 GHz. However, the tested BER of 3.7E-2 significantly exceeded the acceptable threshold of 1E-2. The modulation orders at this bandwidth are limited by the over-all system signal-to-noise ratio as well as the nonlinearity impairment. In Fig. 7, insets (i–iv) depict the signal constellation points for 5-GHz baud rate and the largest transmission baud rate at 150.5-GHz and 210.5-GHz, respectively.

As revealed by Fig. 7, the packaged PD module shows great potential in ultra-broadband and high-speed THz communication in G-band. It is worth mentioning that thanks to the high output power of the PD, high-speed transmission of 90 Gb/s is achieved without any power amplifier after the PD. This helps reduce the complexity and costs of the system, as well as maintaining a high

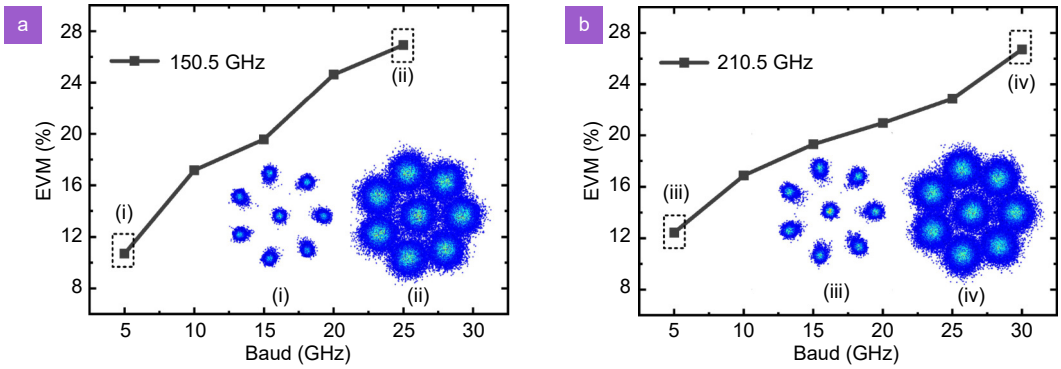

Fig. 7 | EVM performance at different baud rates: (**a**) 150.5-GHz and (**b**) 210.5-GHz.

signal-to-noise ratio (SNR). In our future research, we plan to perform thorough testing at different distances to gain a comprehensive understanding of the performance attributes of our MUTC-PD, so as to facilitate the practical application of our system in real-world scenarios.

The baud rate bandwidth demonstrated in the experiment is mainly limited by the frequency range of the electrical devices in the system. By employing electrical devices with wider bandwidth and advanced DSP algorithm such as deep learning-based end-to-end autoencoder methods[39], it is believed that the PD module can support THz signal transmission with even larger bandwidth and higher rate.

Conclusion

We have demonstrated a compact MUTC photodiode module with WR-5 waveguide output. The PD module exhibits a flat response in the frequency range of 140–220 GHz, and is successfully employed for photonic-assisted THz wireless communications. Transmission rates of 75 and 90 Gbps over 1-m free space are demonstrated at 150.5 and 210.5 GHz carrier frequencies, respectively. The over 80 GHz bandwidth of the PD module at G-band promises other broadband applications, such as THz spectroscopy and imaging. Furthermore, with the high saturated output power, the PD module has the potential to achieve high-performance 6G THz wireless communication. In our future research endeavors, we aim to delve deeper into the application capabilities of the MUTC-PD, encompassing high-speed wireless bi-directional communication. Additionally, we envision a framework where both the MZM and PD modules can be seamlessly integrated on-chip, thereby facilitating chip-level wireless data transmission with integrated antennas. This integrated approach holds significant promise for realizing efficient, high-speed, and compact wireless communication solutions across a wide range of applications.

Furthermore, metasurfaces, renowned for their precise control over electromagnetic wave properties, offer the possibility of engineering specific responses to decouple and independently control different wavelengths, incident angles, spin angular momentums (SAMs), and orbital angular momentums (OAMs). This capability holds significant promise for high-capacity THz communications. Recent advancements in metasurface research[40–43], including novel designs and fabrication techniques, enhance their potential applications in THz communication systems. By integrating metasurfaces into THz devices, alongside well-designed PD modules, such as antennas and modulators, we can achieve enhanced beamforming, signal modulation, and processing capabilities. This integration promises to significantly increase communication throughput, reliability, and efficiency in THz wireless networks, paving the way for future high-speed data transmission and communication technologies.

References

1. Yang P, Xiao Y, Xiao M et al. 6G wireless communications: Vision and potential techniques. *IEEE Netw* **33**, 70–75 (2019).
2. You X H, Wang CX, Huang J et al. Towards 6G wireless communication networks: Vision, enabling technologies, and new paradigm shifts. *Sci China Inf Sci* **64**, 110301 (2021).
3. Tonouchi M. Cutting-edge terahertz technology. *Nat Photonics* **1**, 97–105 (2007).
4. Song HJ, Nagatsuma T. Present and future of terahertz communications. *IEEE Trans Terahertz Sci Technol* **1**, 256–263 (2011).
5. Choi Y, Choi JW, Cioffi JM. A geometric-statistic channel model for THz indoor communications. *J Infrared, Milli, Terahertz Waves* **34**, 456–467 (2013).
6. Mittleman DM. Frontiers in terahertz sources and plasmonics. *Nat Photonics* **7**, 666–669 (2013).
7. Kawanishi T. THz and photonic seamless communications. *J Lightwave Technol* **37**, 1671–1679 (2019).
8. Akyildiz IF, Kak A, Nie S. 6G and beyond: The future of wireless communications systems. *IEEE Access* **8**,

133995–134030 (2020).
9. Kumar A, Gupta M, Pitchappa P et al. Terahertz topological photonic integrated circuits for 6G and beyond: A Perspective. *J. Appl. Phys* **132**, 140901 (2022).
10. Kumar A, Gupta M, Pitchappa P et al. Phototunable chip-scale topological photonics: 160 Gbps waveguide and demultiplexer for THz 6G communication. *Nat Commun* **13**, 5404 (2022).
11. Tan YJ, Zhu CY, Tan TC et al. Self-adaptive deep reinforcement learning for THz beamforming with silicon metasurfaces in 6G communications. *Opt Express* **30**, 27763–27779 (2022).
12. Jia RD, Kumar S, Tan TC et al. Valley-conserved topological integrated antenna for 100-Gbps THz 6G wireless. *Sci Adv* **9**, eadi8500 (2023).
13. Kumar A, Gupta M, Singh R. Topological integrated circuits for 5G and 6G. *Nat Electron* **5**, 261–262 (2022).
14. Yang YH, Yamagami Y, Yu XB et al. Terahertz topological photonics for on-chip communication. *Nat Photonics* **14**, 446–451 (2020).
15. Jia S, Pang XD, Ozolins O et al. 0.4 THz photonic-wireless link with 106 Gb/s single channel bitrate. *J Lightwave Technol* **36**, 610–616 (2018).
16. Yu X, Jia S, Hu H et al. 160 Gbit/s photonics wireless transmission in the 300-500 GHz band. *APL Photonics* **1**, 081301 (2016).
17. Li X Y, Yu J J, Xiao J N et al. Photonics-aided over 100-Gbaud all-band (D-, W-and V-band) wireless delivery. In *42nd European Conference on Optical Communication* 1–3 (VDE, 2016). https://ieeexplore.ieee.org/document/7767627
18. Jia S, Yu XB, Hu H et al. THz photonic wireless links with 16-QAM modulation in the 375-450 GHz band. *Opt Express* **24**, 23777–23783 (2016).
19. Ishibashi T, Kodama S, Shimizu N et al. High-speed response of uni-traveling-carrier photodiodes. *Jpn. J. Appl. Phys* **36**, 6263–6268 (1997).
20. Li QL, Li KJ, Fu Y et al. High-power flip-chip bonded photodiode with 110 GHz bandwidth. *J Lightwave Technol* **34**, 2139–2144 (2016).
21. Morgan JS, Sun KY, Li QL et al. High-power flip-chip bonded modified uni-traveling carrier photodiodes with −2.6 dBm RF output power at 160 GHz. In *2018 IEEE Photonics Conference* (*IPC*) 1–2 (IEEE, 2018); http://doi.org/10.1109/IPCon.2018.8527260.
22. Steffan AG, Margraf M, Rouvalis E et al. High-power InP photodetectors. In *2019 Asia Communications and Photonics Conference* (*ACP*) 1–3 (IEEE, 2019). https://api.semanticscholar.org/CorpusID:211119960
23. Estrella S, Hay K, Campbell J et al. High-power InGaAs/InP MUTC photodetector modules for RF photonics links and ROF. In *Proceedings of the SPIE 10128*, *Broadband Access Communication Technologies XI* 101280M (SPIE, 2017).
24. Jiang CH, Krozer V, Bach HG et ak. Broadband packaging of photodetectors for 100 Gb/s ethernet applications. *IEEE Trans Compon, Packag Manuf Technol* **3**, 422–429 (2013).
25. Runge P, Ganzer F, Gläsel J et al. Broadband 145GHz photodetector module targeting 200GBaud applications. In *2020 Optical Fiber Communications Conference and Exhibition* (*OFC*) 1–3 (IEEE, 2020). https://ieeexplore.ieee.org/document/9083424
26. Shi JW, Huang CB, Pan CL. Millimeter-wave photonic wireless links for very high data rate communication. *NPG Asia Mater* **3**, 41–48 (2011).
27. Ito H, Furuta T, Muramoto Y et al. Photonic millimetre- and sub-millimetre-wave generation using J-band rectangular-waveguide-output uni-travelling-carrier photodiode module. *Electron Lett* **42**, 1424–1425 (2006).
28. Shams H, Fice MJ, Balakier K et al. Photonic generation for multichannel THz wireless communication. *Opt Express* **22**, 23465–23472 (2014).
29. Koenig S, Lopez-Diaz D, Antes J et al. Wireless sub-THz communication system with high data rate. *Nat Photonics* **7**, 977–981 (2013).
30. Lu HH, Tsai WS, Huang XH et al. Transmission of sub-terahertz signals over a fiber-FSO-5 G NR hybrid system with an aggregate net bit rate of 227.912 Gb/s. *Opt Express* **31**, 33320–33332 (2023).
31. Tian YX, Xiong B, Sun CZ et al. Ultrafast MUTC photodiodes over 200 GHz with high saturation power. *Opt Express* **31**, 23790–23800 (2023).
32. Dong YF, de Jesus Fernandez Olvera A, Morales A et al. System integration and packaging of a terahertz photodetector at *W*-band. *IEEE Trans Compon, Packag Manuf Technol* **9**, 1486–1494 (2019).
33. Khani B, Rymanov V, Steeg M et al. Compact E-band (71-86 GHz) bias-tee module for external biasing of millimeter wave photodiodes. In *2015 International Topical Meeting on Microwave Photonics* (*MWP*) 1–4 (IEEE, 2015); http://doi.org/10.1109/MWP.2015.7356673.
34. Khani B, Rymanov V, Flammia I et al. Planar bias-tee circuit using single coupled-line approach for 71–76 GHz photonic transmitters. In *2015 German Microwave Conference* 276–279 (IEEE, 2015); http://doi.org/10.1109/GEMIC.2015.7107807.
35. Sharma AK, Wang H. Experimental models of series and shunt elements in coplanar MMICs. In *1992 IEEE MTT-S Microwave Symposium Digest* 1349–1352 (IEEE, 1992); http://doi.org/10.1109/MWSYM.1992.188254.
36. Mongia R, Bahl I, Bhartia P. RF and microwave coupled-line circuits. *Microwave J* **44**, 390 (2001).
37. Dong YF, Zhurbenko V, Hanberg PJ et al. A D-band rectangular waveguide-to-coplanar waveguide transition using wire bonding probe. *J Infrared, Milli, Terahertz Waves* **40**, 63–79 (2019).
38. Dong YF, Zhurbenko V, Hanberg PJ et al. A D-band rectangular waveguide-to-coplanar waveguide transition using metal ridge. In *2019 IEEE MTT-S International Microwave Symposium* (*IMS*) 1050–1053 (IEEE, 2019); http://doi.org/10.1109/MWSYM.2019.8701099.
39. Li ZY, Dong BY, Li GQ et al. Attention-assisted autoencoder neural network for end-to-end optimization of multi-access fiber-terahertz communication systems. *J Opt Commun Networking* **15**, 711–725 (2023).
40. Li X, Chen LW, Li Y et al. Multicolor 3D meta-holography by broadband plasmonic modulation. *Sci Adv* **2**, e1601102 (2016).
41. Li Y, Li X, Chen LW et al. Orbital angular momentum multiplexing and demultiplexing by a single metasurface. *Adv Opt Mater* **5**, 1600502 (2017).
42. Guo YH, Zhang SC, Pu MB et al. Spin-decoupled metasurface for simultaneous detection of spin and orbital angular momenta via momentum transformation. *Light Sci Appl* **10**, 63 (2021).
43. Li XY, Chen C, Guo YH et al. Monolithic spiral metalens for ultrahigh-capacity and single-shot sorting of full angular momentum state. *Adv Funct Mater* **34**, 2311286 (2024).
44. Ito H, Furuta T, Ito T et al. W-band uni-travelling-carrier photodiode module for high-power photonic millimetre-wave generation. *Electron Lett* **38**, 1376–1377 (2002).

Acknowledgements

This work was supported in part by National Key Research and Development Program of China (No. 2022YFB2803002); National Natural Science Foundation of China (Nos.62235005, 62127814, 62225405, 61975093, 61927811, 61991443, 61925104 and 61974080); and Collaborative Innovation Centre of Solid-State Lighting and Energy-Saving Electronics.

Competing interests

The authors declare no competing financial interests.

Scan for Article PDF